Microstructural analysis and electro-optic properties of thick epitaxial math xmlns="http://www.w3.org/1998/Math/MathML">mrow>msub>mi>BaTiO/mi>mn>3/mn>/msub>/mrow>/math> films integrated on silicon (001)

Marc Reynaud, Zuoming Dong, Hyoju Park, Wente Li, Agham B. Posadas, Jamie H. Warner, Daniel Wasserman, and Alexander A. Demkov

Phys. Rev. Materials **6**, 095201 — Published 2 September 2022

DOI: 10.1103/PhysRevMaterials.6.095201

Microstructural analysis and electro-optic properties of thick epitaxial $BaTiO_3$ films integrated on silicon (001)

Marc Reynaud[a], Zuoming Dong[b], Hyoju Park[c], Wente Li[a], Agham B. Posadas[a], Jamie H. Warner[c], Daniel Wasserman[b] and Alexander A. Demkov[a1]

[a]Department of Physics, University of Texas at Austin

[b]Department of Electrical and Computer Engineering, University of Texas at Austin

[c]Walker Department of Mechanical Engineering, University of Texas at Austin

Abstract

Recent advances in epitaxial oxide deposition have enabled the fabrication of thick films of ferroelectric perovskite $BaTiO_3$ capable of providing a robust electro-optic response via the Pockels effect in silicon photonic devices. We report a microstructure analysis of such films integrated on Si(001) by molecular beam epitaxy, showing how the crystallographic and polarization orientation change as a function of thickness. The measured electro-optic properties of the film correlate well with the microstructural analysis and demonstrate the potential of Si-integrated $BaTiO_3$ for silicon photonics. An effective Pockels coefficient of up to 268 pm/V has been demonstrated in 110-nm-thick films in transmission measurements and 352 pm/V in waveguide measurements.

Introduction

Silicon-integrated photonics has seen a recent surge in research activity as a potential successor to various aspects of modern electronics technology. Photonic devices have been shown to be a viable solution to quantum, cryogenic and neuromorphic computing [1-3], as well as chip-to-chip interconnects [4,5]. However, modulating light in Si by itself has proven to be difficult, one of the reasons being that unstrained Si does not have a linear electro-optic response, also known as the Pockels effect. Even when strained, Si only exhibits a very small Pockels response [4]. Optical switches have been fabricated on Si using other physical phenomena but these have drawbacks that are difficult to deal with. For example, the plasmon dispersion effect modulates the absorption coefficient and therefore the intensity of light through a waveguide [4], while the thermo-optic effect is a relatively high-power consumption effect that suffers from low switching speeds [4,6]. Due to these limitations, much work has been done to integrate materials with a large Pockels response onto Si, and the material with the largest known response is $BaTiO_3$ (BTO). Recent work on making electro-optical (EO) modulators based on the Pockels effect in BTO showed a Pockels tensor component of approximately 923 pm/V [7]. This is substantially larger than the current

[1] demkov@physics.utexas.edu

industry standard material used for EO modulators, $LiNbO_3$ (LNO), which has a Pockels response of approximately 32 pm/V [8,9]. LNO is difficult to integrate onto Si due to the need for a complex and expensive wafer bonding process [10, 11]. Currently, it stands as the most established technology in the field with low propagation losses [12]. But with a substantially larger Pockels response that can lead to much shorter, lower power devices, BTO poses itself as the next generation beyond LNO for advancing the field of silicon-integrated photonics [7, 13].

While thick films of BTO on Si of varying quality have been grown to study the EO properties of the material [14], careful structural analysis and crystallographic orientation control have been largely limited to thinner films [15,16]. Hsu et al. [17] investigated the effect of varying the $SrTiO_3$ (STO) buffer layer thickness on orientational control of thick BTO films. While some work has been done to compare different growth techniques of thick film BTO on Si [18,19], more in-depth materials analyses need to be performed on thicker films to fully understand the properties of the films used for realistic integrated device geometries. By performing careful materials analysis on thick molecular beam epitaxy (MBE)-grown films, we further the research into BTO-enabled Si-integrated photonics by providing an understanding of the structure-property relationships of these films. One important detail to consider is the orientation of ferroelectric polarization domains in thick BTO films on Si. Most reported EO modulators employ the so-called hybrid approach [20]. In hybrid structures, the waveguides are fabricated in Si or SiN_x deposited on BTO that has been integrated on Si. Due to the refractive index difference between the waveguide and the BTO only a portion of the guided mode leaks into BTO where it is modulated. In such hybrid EO modulators, it is preferable to have the polarization of BTO pointing parallel to the surface of the Si wafer (a-axis BTO) versus being perpendicular to it (c-axis BTO) [21]. The former matches the device geometry of X- or Y-cut LNO devices [22]. This device orientation preference has been confirmed by both waveguide modelling and in experimental waveguide geometries [7,21]. Speck et al. [23,24] have previously investigated theoretically the accommodation of strain in epitaxial BTO films by misfit dislocation formation. They show that various ferroelectric domain patterns can occur as the film is cooled from the growth temperature to room temperature through the ferroelectric phase transition depending on cooling rate and the presence of depolarizing fields, accounting for both thermal expansion and lattice mismatch.

In this paper, we describe the MBE growth of thick high-quality single-crystalline BTO films on Si (001) and present a rigorous microstructure analysis of 110 nm films. Scanning tunneling electron microscopy (STEM) images are taken, and geometric phase analysis (GPA) of the STEM images is performed to investigate the domain structure and local strain in the film as a function of layer position in the film, which show that the crystallographic orientation of the film begins primarily in the out-of-plane (c-axis) orientation before switching to in-plane (a-axis) orientation. These results are compared with phase field modelling of the BTO films, which confirms the transition of the crystallographic orientation from primarily c-axis to primarily a-axis BTO. We fit x-ray diffraction measurements of these films, with information obtained from GPA taken into account in order to constrain the XRD analysis. In addition, we measure the electro-optic response

of the films, using both transmission and waveguide geometries, which provides additional evidence for the crystallographic re-orientation as a function of thickness. We find the average effective Pockels coefficient for MBE-grown BTO on Si to be 223 pm/V with a maximum of 268 pm/V in transmission geometry, and 352 pm/V in waveguide geometry. The research presented here was done on five identically grown BTO films on 2" Si wafers, apart from the waveguide measurement that used BTO grown on a silicon-on-insulator wafer. The characterization results between the different wafers are very similar, and as such a representative set of data was used in the manuscript.

Film Growth

First, a double-side-polished two-inch Si wafer is degreased in acetone, isopropanol and water. Then, it is exposed to UV ozone for approximately 15 minutes to remove hydrocarbon residue from the surface. The wafer is then loaded into a vacuum transfer line that is connected to both a DCA 600 oxide molecular beam epitaxy (MBE) growth chamber that can achieve base pressures in the 10^{-10} torr with an attached Staib reflection high energy electron diffraction (RHEED) apparatus and a kSA 400 imaging system, and to an x-ray photoelectron spectroscopy (XPS) chamber with a VG Scienta R3000 hemispherical analyzer that uses monochromated Al Kα X-rays.

Before the growth of BTO, a buffer layer of $SrTiO_3$ (STO) is first grown on the wafer since an STO buffer is necessary to grow BTO epitaxially on Si [25,26]. However, a thin layer of native SiO_2 is first removed from the Si surface using Sr-assisted oxide desorption, which has been described extensively elsewhere [27]. Once the SiO_2 layer has been removed, ½ monolayer (ML) of Sr is deposited on the Si surface, leaving the desired 2x1 reconstruction of the Si surface that we can deposit STO on without re-oxidizing Si [28]. For STO growth, the film is cooled to 200 °C and a 2 nm seed layer of STO is first grown by co-deposition of Sr and Ti (evaporated from effusion cells), with molecular oxygen being slowly ramped up during the growth. The oxygen source is ramped up from a pressure of approximately 8×10^{-8} torr to a pressure of 5×10^{-7} torr during the growth. The Sr and Ti fluxes are measured using a quartz crystal monitor (QCM) prior to growth. This seed layer process produces an amorphous layer of STO, which is then heated to approximately 550-650 °C to crystallize it. It is important to note that the oxygen should be shut off during the crystallization process so as to not allow oxygen to diffuse through the amorphous STO and react with the Si surface below to form new SiO_2 before STO is crystallized. Once crystallized, additional STO (2-3 nm) is grown using co-deposition to increase the quality of the STO buffer layer. This additional STO is grown at 550 °C and 5×10^{-7} torr of oxygen. After the completion of the STO layer, BTO is then grown using shutter deposition from the Ba (also a Knudsen cell) and Ti sources with the growth pressure raised to 5×10^{-6} torr, and the growth temperature raised to 750 °C. The BTO is grown in cycles of 10 nm coupled with 10-minute intermediate anneals to ensure a high crystal quality. The film growth is monitored with RHEED, with a typical image shown in Figure 1a. Growth is paused after 5 cycles (50 nm) to remeasure Ba and Ti rates and to perform in situ XPS to check the composition of the film, readjusting the

relative rates of Ba and Ti as needed to maintain stoichiometry. The heating and cooling rates used during growth are 50℃/min, except when for heating the amorphous STO layer to crystallize it, in which case the heating rate is 20℃/min.

After growth, general materials characterization is done on the film to ensure both compositional and crystalline quality. XPS is used to check the composition of the BTO film at multiple thicknesses, checking that the Ba:Ti ratio was within 5% of a 1:1 ratio at each thickness measured, and is shown in Supplemental Material Note I [29]. X-ray diffraction (XRD) characterization using a Rigaku Ultima IV diffractometer was then performed to determine the crystallographic orientation and the crystal quality, which are shown in Figures 1b and 1c. The out of plane diffraction (Figure 1b) shows that the film is in the expected phase, with no diffraction signal from BTO 101 or 111. The Si 002 peak and its side shoulder are due to multiple diffraction effects, and were found to vanish when the sample was rotated azimuthally away from a high symmetry direction [30]. The rocking curve around the 200/002 peak (Figure 1c) shows that the film is of high quality for a film grown on Si, with a FWHM of $\Delta\omega \sim 0.28°$. This is comparable to the state-of-the-art BTO used in Abel et al. [7], and better than films of comparable thickness on Si reported by others [17,19]. X-ray reflectivity analysis for the film yields a BTO thickness of 107 nm for a film that is nominally 110 nm. For electro-optic measurements, metal contact pads were deposited on the BTO films using a photolithographic lift-off process and DC sputtering, as seen in Reynaud et al. [31]. The process patterns contact pads with gaps at different angles with respect to the BTO crystalline c-axis or polar axis, which is in-plane for a-axis BTO, and for this experiment contacts with gaps 45° with respect to the BTO polar axis are used, which can be used to apply a poling voltage to the film. Films are annealed at high temperature, 750-800° C ex-situ in oxygen to anneal oxygen vacancies before contacts are deposited.

Microstructure analysis

In addition to x-ray diffraction, we have performed cross-sectional annular dark-field scanning transmission electron microscopy (ADF-STEM) imaging to analyze in detail the crystalline structure of the BTO films. The cross-sectional samples for scanning transmission electron microscopy (STEM) were fabricated using a Scios 2 HiVac focused ion beam system from Fisher Scientific. ADF-STEM was performed using a JEOL NEOARM equipped with a probe corrector for STEM, operated at an accelerating voltage of 200 kV. ADF-STEM images were carefully calibrated using the silicon lattice spacing under the BTO/STO layer in two orientations; one image is taken parallel to Si [110] direction, and the other along [001], to minimize the error from camera scanning. With this technique, we are able to examine the epitaxy between the different layers in the heterostructure. Figure 2a is a large-scale cross-sectional ADF-STEM image showing all layers of the heterostructure, while Figure 2b is a magnified image showing the interface regions between the layers. Both images are taken along the [110] direction of Si, but because STO and BTO both grow with 45° rotation to Si [110], the images correspond to the [100] direction of STO and BTO. The wide scale image (Fig. 2a) shows the film has no distinct grains, while the magnified image (Fig. 2b) shows high quality epitaxy between the layers and very sharp interfaces. Defects can be

seen, which are regions of strain relaxation in the deposited layers. Figure 2c shows the epitaxy between the layers (excluding interfacial SiO_2).

Geometric phase analysis (GPA) was performed on the STEM images to extract information regarding the local orientation of the BTO crystal as a function of layer position; the GPA data are shown in Figure 3. GPA was performed in Digital Micrograph using Koch's FRWR tools plugin [32], which is based on the methods of Hÿtch et al. [33]. GPA maps were made at different magnifications and image orientations to confirm they have the same strain maps at different conditions. The inverse of the g-vector in the *x*-direction used for GPA maps are multiplied to the GPA maps and then added using ImageJ to transform the strain maps to lattice parameter maps. Each of the ε_{xx} of the GPA maps - one parallel to Si [110] direction (in-plane) and the other along Si [001] direction (out-of-plane) is used to exclude the lattice distortion that might come from the scanning error along the *y*-direction. This information is of particular interest because only BTO with in-plane polarization will contribute to the Pockels effect in the free space transmission geometries used for Pockels coefficient measurements, and also in the most commonly used waveguide geometries relevant to Si photonics applications [19, 21]. Figure 3a shows the region of the film where GPA was performed, and Figures 3b and c show strain in the *x*- and *y*-direction, ε_{xx} and ε_{yy}, respectively. The strain in the film relative to Si comes from two different effects, as described in [34]. First, the film experiences a compressive strain due to the lattice mismatch between BTO and Si, about 4.5%. This is somewhat alleviated by the STO buffer layer, but not entirely. However, there is a large thermal expansion mismatch between the BTO and Si, with BTO around 14.2×10^{-6} J/K and Si 4.26×10^{-6} J/K at 700 °C [35,36]. During the cooling process immediately after film growth, the thermal expansion mismatch leads to an in-plane tensile stress being applied to the BTO because the Si does not shrink as quickly as the BTO. These two sources of strain will influence the film crystallographic orientation, which starts out as c-axis orientation before gradually changing to a-axis orientation as the film gets thicker. The region in which the average lattice constants are extracted is outlined in white boxes, with an arrow showing the path along which the lattice constants are measured. The result of the lattice constant extraction is shown in Figure 3(d-e). It is seen that the film starts off c-axis oriented before gradually transitioning to being in the a-axis orientation. We find that there is a region approximately 30 nm thick that is c-axis oriented, and then a transition region of approximately 20 nm. Beyond this, the film becomes a-axis oriented. By assuming the transition region to be half a-axis and half c-axis, we see that for a 110-nm BTO film grown by MBE on Si, we have approximately 36% c-axis and 64% a-axis orientation. The variation in the x-direction GPA map is likely due to how to the strain relaxes at different points in the x-direction along the film, primarily due to the location of defects causing strain relaxation. We think the modestly sized scan window of around 40 nm wide in the x-direction for the lattice constants captures an average value of the lattice constant which encapsulates this effect. The error in the data processing yields an error of approximately ±0.05 Å, which is larger than the resolution of different lattice orientations for BTO, but the general trend in the data is reliable.

In order to gain further insight into the domain morphology of both strain and polarization in BTO as a function of thickness, we use phase field simulations (PFSs) that are based on a phenomenological BTO free energy model [37,38,39]. The domain morphology of a BTO thin film under specific mechanical and electrical boundary conditions can be described by the Landau-Khalatnikov (LK) equation, $\beta \frac{\partial P_i}{\partial t} = -\frac{\delta F}{\delta P_i}$, along with the utilization of electrical and mechanical equilibrium equations [38,39,40]. We employ the finite element method to implement the PFSs and solve the BTO thin film free energy model. Using this, we can study the polarization and strain distribution across the simulation cell, enabling a direct quantitative comparison with the results from GPA of the STEM images. This is particularly useful since the strain distribution across the film can be quite complicated [38]. In order to compare with experiments, it is essential to employ appropriate strain boundary conditions, because thick BTO films on Si undergo a progressive strain relaxation [19,34] originating at the STO/BTO interface that gradually relaxes as the films get thicker. Considering the results from the analysis of the STEM and GPA data (Fig. 3), we assume the strain relaxation process to be approximately linear as a function of thickness, as indicated by Fig. 4a. We set the compressive strain value at the interface of the STO/BTO to the values extracted from GPA shown in Fig. 3d and e. Simulation details and boundary conditions can be found in the Supplemental Material Note II [29] of this work and that of Refs. [31,39]. Fig. 4b-c show the strain maps of ε_{xx}, ε_{yy} and ε_{zz}, as well as the corresponding in-plane and out-of-plane lattice parameter distribution, where we can clearly observe the transition area from c-orientation to a-orientation. As the polarization points along the long axis (c-axis) of *4mm* BTO, this also indicates a change in polarization direction from out-of-plane to in-plane. In the PFS results, the two possible orientations (long axis along either *x* or *y* direction) of an a-domain are clearly seen, indicating film relaxation relative to Si. Fig. 4d displays the plane-averaged lattice parameters along the *z* direction. In the PFS results, the a-domain volume is about half of the simulation cell, while the c-domain and transition areas each take up about a quarter of the simulation cell, which agrees well with GPA results in Fig. 3. Please note that the GPA maps only include ε_{xx} and ε_{yy} as the in-plane and out-of-plane strain while the PFS include ε_{xx} and ε_{yy} as the two in-plane strains and ε_{zz} as the out-of plane strain.

Using the information found from both the STEM analysis and PFS, we can now fit the out-of-plane XRD peaks of the 002 and 004 regions, which are shown in Figures 5a and 5b, respectively. Considering the domain fractions found using GPA from the STEM images, we can approximate the area fractions with more confidence. We find that there is a portion of the film that is nearly commensurate to the STO/Si, indicated by the red curve in the figures. This region is strained c-axis oriented. This peak is difficult to fit because it has a different shape than the other peaks and is small compared to the others, however, there is a clear shoulder on the scans indicating its presence. The main curve is fit with two peaks, corresponding to the 002/200 peaks and the 004/400 peaks of BTO. The peaks are fit using the pseudo-Voigt 1 function in Origin 2020 and constraining the peak shape profile and FWHM for the main peaks to be the same but allowing the

smaller side peak FWHM to vary. The area, peak center position and offset were also allowed to vary. Considering the results of the GPA analysis, we say that the green curve main peak (left main peak) is the relaxing mixed c/a-axis portion of the film, while the blue curve (right main peak) is the a-axis region. Using this, we can calculate the average lattice constants and domain fractions for the different orientations. The lattice constants are listed in Table I. While the lattice constants are somewhat large compared with the expected values for bulk a-axis BTO, when compared with our GPA analysis and the strong electro-optic response seen (next section), we can confidently say that this film has a substantial a-axis domain fraction. The domain fraction is calculated by taking the area of the a-axis peak plus half of the relaxing mixed c/a-axis peak and dividing that by the total area under the curve. For the 002/200 region, we find a domain fraction of 72:28 a:c and for the 004/400 region, 74:26 a:c. The domain fraction values are within a reasonable variation when compared with the GPA analysis, which indicates that constraining the FWHM and peak shape profile while allowing the other function parameters to vary is a reasonable method of fitting for films grown with this method. It should also be noted that the STEM analysis is only performed in one spot on the film, and it is likely that there is local variance if we were to take images of other spots. XRD on the other hand, is an average over a large portion of the film. With this analysis, we can use the correlation between GPA and XRD fitting techniques to fit BTO films grown using the same process. Along with out-of-plane XRD, in-plane XRD scans of the 004/400 region were done on the films to investigate the in-plane orientation. For the in-plane scan, the polarization direction can go in two perpendicular in-plane orientations. By scanning along one azimuth, one thus expects to see both a short and long lattice parameter, 400 and 004. The peak positions in the in-plane alignment lack a reference to the Si beneath and may have a small offset. However, the peaks are definitely split, which indicate that the film contains two in-plane spacings. The peak in the higher angle 400 position being larger is likely due to two effects. One, the in-plane scan can penetrate through enough of the film to see a portion of the c-axis oriented BTO further down. Two, the slight difference in structure factor due to the Ti displacement is expected to cause a slight intensity reduction in the lower angle peak. The scan is shown below in Figure 5c and the extracted lattice constants in Table I.

From the STEM images, we see that BTO thin films can be maintained with high uniformity throughout the film growth process. GPA analysis of the films shows the expected crystallographic orientation evolution as the film gets thicker, transitioning from a c-axis oriented to become more a-axis oriented as the film grows thicker. PFSs with the same initial conditions as seen in GPA indicate a similar relaxation process. However, there is some variability in how the evolution occurs, which means that the two determining factors discussed previously [34] have a complicated interplay. In some regions of the film, the thermal expansion mismatch between the layers has a stronger influence on the film and the film grows as a-axis almost immediately. In other regions, the compressive strain dominates before the thermal expansion comes into play. Lastly, there are defects which appear to trigger rapid strain relaxation. Combining the GPA and PFS analysis, we were able to perform peak fitting for the BTO out-of-plane 002/200 and 004/400 scans by approximating the area ratio between the two peaks as the volume fraction of the two

crystallographic orientations. The in-plane XRD of the 004/400 gives confirmation of in-plane domains with 90° rotation between them.

Electro-optic characterization

Having seen from STEM GPA and XRD analyses that our $BaTiO_3$ films are partially in-plane polarized, we now proceed to measure the Pockels coefficient of these films. The linear electro-optic effect is the first order change in the index of refraction with respect to an applied electric field, which is given as

$$n_{ij}(E) = n_{ij}(0) - \frac{1}{2} {n_{ij}}^3(0) \sum_k r_{ijk} E_k \tag{1}$$

where the index *k* identifies the direction of the applied external electric field and the sum over the repeated index is assumed [41]. The Pockels coefficient r_{ijk} indicates the strength of the response in a material in a given geometry of physical parameters. These coefficients are tied to the point group symmetry of the crystal. This means that by applying an external electric field, we are able to modify the index ellipsoid of the film, $\sum_{ij}(1/n_{ij}^2)x_i x_j = 1$, either by rotation of the ellipsoid or by distorting it. The term $\sum_{ij}(1/n_{ij}^2)$ is called the impermeability and is denoted by η_{ij}. This allows us to write Eq. (1) as

$$\eta_{ij}(E) = \eta_{ij}(0) + \sum_k r_{ijk} E_k \tag{2}$$

,

For *4mm* BTO, we can rewrite the second term on the right-hand side (RHS) of Eq. (2) in a useful matrix form. From [41], the nonzero Pockels components for *4mm* symmetry are given by (in contracted Voigt notation):

$$r_{ijk} = \begin{pmatrix} 0 & 0 & r_{13} \\ 0 & 0 & r_{13} \\ 0 & 0 & r_{33} \\ 0 & r_{42} & 0 \\ r_{42} & 0 & 0 \\ 0 & 0 & 0 \end{pmatrix} \tag{3}$$

Note the symmetry relations $r_{42} = r_{51}, r_{13} = r_{23}$ which come from the symmetry of the BTO *4mm* structure. This allows us to rewrite the RHS second term of Eq. (2) in matrix form as

$$\Delta\eta_{ij}(E) = \begin{pmatrix} r_{13}E_3 & 0 & r_{42}E_1 \\ 0 & r_{13}E_3 & r_{42}E_2 \\ r_{42}E_1 & r_{42}E_2 & r_{33}E_3 \end{pmatrix} \tag{4}$$

We should note here that, similar to other optical phenomena, the principal axis formulation is generally given for the Pockels effect, that is, axis 3 is the polar axis of the crystal. For BTO, this points along the $\vec{c}$ or long axis of the crystal. As shown in Abel et al. [14], the orientation of the

applied electric field in BTO thin films that gives the largest response is at 45° with respect to the crystalline c-axis in either of the two possible in-plane domain orientations for a-axis oriented BTO. This orientation allows the r_{42} component of BTO to be utilized, which has been shown to be approximately 1300 pm/V in bulk [42] and 923 pm/V in 225 nm thin films [7]. If the external electric field is applied at 0° to the c-axis (E_3) one would expect the largest coupling, but oppositely oriented domains perpendicular to applied field will have electro-optic modulations that cancel out [43], and this is seen for the 0° pads in [14], which can only couple with r_{33} and r_{13}.

The setup used for the Pockels measurement is illustrated in Figure 6a and the important quantities to consider are shown in Figure 6b. With the transmission geometry in our setup, the polarization of the film must be in-plane in order to interact with the light, which propagates out of plane. If the film has out of plane polarization, then the polarization orientation cannot normally be changed to in-plane polarization by an external electric field [16], and regions of oppositely oriented polarizations will produce phase shifts that deconstructively interfere with one another when poled in this geometry [19,43]. A short description of the experiment is given here, while a full description can be found in [30]. The measurement is performed by applying a 40-45 V DC bias to the film via a Keithley 2612B Source/Measure Unit, with a 5 V_{rms} modulating AC voltage (100 kHz) applied on top of that via an SRS 830 Lock-In Amplifier. The separation between the metal pads is 7 μm. To ensure that the BTO is not shorting, I-V measurements were done beforehand, and an exemplary I-V curve is shown in Supplemental Material Note III [29]. A Neophotonics PPCL600 laser produces light at 1550 nm. As the light passes through the film it becomes slightly elliptical by acquiring a phase shift, which is then compensated for by the quarter-wave plate and relinearized with a characteristic polarization rotation $\delta/2$. It then goes through an analyzer which is rotated by θ_a. The light is then collected by a Thorlabs PDA10CS2 photodetector, also attached to the Keithley and lock-in amplifier. The Keithley measures the direct power P, while the lock-in amplifier measures the modulated power ΔP. This phase shift depends on the active film thickness l. The tungsten contact pad angle ϕ_E must also be considered, as it determines the direction of the applied electric field.

As stated previously, the largest Pockels coefficient for *4mm* BTO is the r_{42} component, which is optimally coupled in this geometry by applying the electric field at 45° with respect to the crystalline c-axis. Therefore, the tungsten contact pad angles used for this experiment are in this geometry. Figure 6c shows an example fit of $\Delta P/P$, from which the coefficient $\delta/2$ can be extracted and is used to find the effective Pockels coefficient. The equations used in fitting are shown as an inset. Using this, we can calculate an effective Pockels response by taking our max phase change to be $2(\delta/2)$ [31] and writing

$$\phi = 2\,(\delta/2) = k\Delta n(E)l = \frac{2\pi n_0^3 r_{eff} E_{a.c.} l}{2\lambda_0} \rightarrow r_{eff} = \frac{2(\delta/2)\lambda_0}{\pi n_0^3 E_{a.c.} l v} \tag{5}$$

Where λ_0 is the wavelength of the laser, n_0 is the average index of BTO (2.28) [44], $E_{a.c.}$ is the applied A.C. electric field (approximated as a parallel plate capacitor [7, 13, 31]), l is the thickness

of active BTO film (a-axis), and υ is a geometric factor accounting for how much of the film is Pockels active in this geometry, which is 1 for this measurement. From the GPA and XRD analyses, we know that the film is not entirely a-axis oriented. If we use the approximations found in the XRD analysis to estimate the domain fraction, we can say that the film is approximately 74% a-axis oriented. For a 107 nm thick film, this is ~80 nm. We find the maximum Pockels response from this film to be approximately 268 pm/V when a 45° pad is measured and the input angle is varied. The average Pockels response measured over multiple pads is 223 ± 27 pm/V when averaged over the peaks of multiple 45° pads, where the error is one standard deviation. The film shows a dependence on input polarization as shown in Figure 6d, confirming that the response we are seeing is from the Pockels effect. It is important to note that there is a point on the input angle curve where a Pockels coefficient close to 0 pm/V is seen, which is a good indication that the response seen here is from the Pockels effect. A drive field measurement that also supports this statement can be found in Supplemental Material Note III [29]. The films were poled at 40-45 V for ~10 minutes before measurement.

Along with transmission measurements of the electro-optic response of our BTO thin films, waveguide measurements were also performed. BTO films using the same growth technique described above are deposited on silicon-on-insulator (SOI) substrates comprised of a ~2 μm buried oxide (BOX) below a 16 nm Si device layer. The thick BOX layer, in unison with the thin, high-index Si, provides the necessary index contrast to confine the optical mode. An oxidized Si ridge patterned on top of the BTO guides the optical mode, the profile of which is shown in Figure 7a. Details of the waveguide processing and simulation can be found in Supplemental Material Note IV [29]. As shown in the figure, the mode profile of the guided wave (at 1550 nm) extends over the different layers of the waveguide, so an effective index of refraction is used for calculations [13] and only a portion of the mode will be confined in the modulating BTO. The waveguides are patterned to create Mach-Zehnder interferometers. Images of the waveguides are shown in Figure 7b. The Mach-Zehnder interferometers are used to measure the electro-optic response of the BTO thin film. In the Mach-Zehnder geometry, a waveguide is split into two arms, one of which has an electric field applied to it. By applying a field, the index of the BTO is modulated which causes the light confined in that arm to either speed up or slow down relative to the unmodulated arm. When the arms reconnect, the light from the two arms have a shifted phase relative to one another which causes partial deconstructive interference. The specific applied voltage where the light from the two arms completely deconstructively interfere with one another (π phase shifted) is called the half-wave voltage V_π. This value multiplied by the length of the modulator arm it takes to accomplish this modulation, $V_\pi L$, is generally used as a characteristic parameter of an electro-optic modulator. The equation for the modulation of intensity in an integrated Mach-Zehnder interferometer is [45]

$$I = I_0 \cos\left(\frac{\Delta\phi}{2}\right)^2 \tag{5}$$

$$\Delta\phi = \frac{\Gamma 2\pi r_{eff} n_{eff}^3 VL}{2\lambda_0 d} \quad (6)$$

Where $\Delta\phi$ is the phase shift, Γ is the overlap of the mode with the modulating portion of the film (a-axis BTO), r_{eff} is the effective Pockels coefficient, n_{eff} is the effective index, V is the applied voltage, L is the length of the interferometer arms, 500 μm, λ_0 is the wavelength of light used, 1550 nm, and d is the electrode gap, 8 μm. Similar to transmission measurements, the electric field is considered to be very close that of a parallel plate capacitor [7,13,31]. Further details on the Mach-Zehnder measurements can be found in [45]. Gratings were designed to in-couple 1550 nm light to the waveguide at an 8° incidence angle and also at the end to out-couple light. Fiber probes with 8° inclination angle were used for coupling 1550 nm light from a Thorlabs S4FC1550 single mode laser into the waveguide at one end and collecting output light from the other end of the waveguide through similar grating couplers. The output light was then detected by a Thorlabs PDA10CS photodiode and signal was sent into the lock-in amplifier synchronized to the function generator which modulates the laser source at 1000 Hz with a 50% Duty cycle. To obtain the electro-optical modulation amplitude, we used a GSG probe applying DC biases to one arm and recorded lock-in amplifier signal at different voltages. The sample was first poled at -60V for 10 minutes, and measured from -40 to 40 V with 0.5V step size. At each voltage, different integration time was set to check if any slow modulation effect was omitted.

The sample used for waveguide measurements is 200 nm of BTO grown with the same process as the sample for STEM and transmission electro-optic measurements, on a 16 nm device layer Si layer SOI substrate. The XRD pattern for the 004/400 region of the film is shown in Figure 7c, with additional XRD found in Supplemental Material Note IV [29]. The films grown on SOI with this method typically do not show the strained c-axis orientation to start, but they do have a noticeable signal for a peak that corresponds to unstrained c-oriented BTO, before beginning to relax. Similar to the analysis done for films grown on bulk Si, we fit the left feature with two components while the right feature is the more relaxed a-axis peak that we fit with one component. Taking the a-axis fraction to be the sum of half of the relaxing c/a-axis peak and the a-axis peak, we find the a-domain fraction to be approximately 59:41 a:c. With this, we calculate the overlap Γ of the a-axis portion of the film to be about 31.6%. The results of the Mach-Zehnder interferometer measurements are shown in Figure 7d, where we plot the lock-in amplifier signal vs. applied voltage. We can see a modulation from very close to maximum signal to no signal which indicates fully deconstructive interference. One also notes a drop in signal at very low voltages, especially towards small positive voltage. Repeated measurements yield consistent results. The unexpected dip in the intensity as the film is being modulated is possibly due to the presence of an uneven distribution of pinned ferroelectric domains along the two waveguide arms with 90° rotated polarity that causes destructive interference. It is also possible due to absorption from trapped charges. Discontinuities in the film resistance manifest in the I-V characteristics at the voltages at which the dip occurs, as seen in Supplemental Material Note IV [29]. From this data we can extract the modulation values due to the Pockels effect. The value for $V_\pi L$ can be found by directly taking

the voltage difference to get the lock-in intensity from maximum to minimum, which is ~30 V. To get this, we used the peak position of the fit and the minimum signal points extracted during measurement. The length of the arm being modulated is 500 μm. This gives us a $V_\pi L$ of 1.5 V·cm with an electrode gap of 8 μm. When normalized with respect to contact spacing, this is competitive with other state-of-the-art devices found in literature; a list of values is shown in Table II [7,13]. From Eq. 6, we extract an r_{eff} of approximately 352 pm/V. The larger r_{eff} than transmission measurements is likely due to either the film having a larger a-axis fraction being modulated for the thicker film, from a difference in geometry between the two experimental setups, or from a difference in tetragonality between the films [19].

The Pockels response seen in the transmission and waveguide measurements is comparable to or even stronger than that seen in prior work for films of similar thickness [7,13,19]. In the waveguide structure, we see that the $V_\pi L$ value normalized to the electrode gap is comparable to the top-of-the-line electro-optic devices in BTO on Si. This indicates that our films are of high quality and gives good indication that films grown with our technique are capable of being used in high performance electro-optical components.

Conclusions

Thick MBE-grown BTO films of about 110 nm were characterized in depth with XRD and STEM imaging analysis to gain insight into how these films grow and relax on silicon. The strain relaxation seen in GPA gives a similar result to what is obtained with phase field modelling when using similar boundary conditions. The GPA and XRD analyses show similar results to one another and corroborate with the transmission and waveguide electro-optic data that indicates the film has a sizable Pockels response. This effective electro-optic response in transmission of 223 pm/V (average) and 268 pm/V (maximum), along with 352 pm/V in waveguide geometry that is comparable to or even larger than what has been seen for BTO films of comparable thickness on Si. This is also substantially larger than LNO's electro-optic response of about 32 pm/V [8,9,41]. This work provides valuable insight into the use of BTO in silicon-integrated photonic devices because it shows how the strain and orientation evolve with film thickness for high quality BTO films on silicon and its relationship with the measured electro-optic response.

Acknowledgements

We thank Wei Guo and Tess Paoletta for insightful discussions and critical reading of the manuscript. The work is supported by the Air Force Office of Scientific Research under grant FA9550-18-1-0053.

References

1. K. Vandoorne, P. Mechet, T. V. Vaerenbergh, M. Fiers, G. Morthier, D. Verstraeten, B. Schrauwen, J. Dambre, and P. Beinstman, Nat. Commun. **5,** 3541 (2014).

2. F. Eltes, G. E. Villarreal-Garcia, D. Caimi, H. Siegwart, A. A. Gentile, A. Hart, P. Stark, G. D. Marshal, M.G. Thompson, J. Barreto, J. Fompeyrine, and S. Abel, Nat. Mater. **19,** 1164 (2020).
3. G. Z. Mashanovich, Nat. Mater. **19,** 1135 (2020).
4. G. T. Reed, G. Mashanovich, F. Y. Gardes, and D. J. Thomson, Nat. Photonics **4,** 518 (2010).
5. M. J. R. Heck, H. W. Chen, A. W. Fang, B. R. Koch, D. Liang, H. Park, M. N. Sysak, and J. E. Bowers, IEEE J. Sel. Top. Quantum Electron. **17,** 333 (2011).
6. Y. Kim, J. H. Han, D. Ahn, and S. Kim, Micromachines **12,** 625 (2021).
7. S. Abel, F. Eltes, J. E. Ortmann, A. Messner, P. Castera, T. Wagner, D. Urbonas, A. Rosa, A. M. Gutierrez, D. Tulli, P. Ma, B. Baeuerle, A. Josten, W. Heni, D. Caimi, L. Czornomaz, A. A. Demkov, J. Leuthold, P. Sanchis, and J. Fompeyrine, Nat. Mater. **18,** 42 (2019).
8. A. K. Hamze, M. Reynaud, J. Geler-Kremer, and A. A. Demkov, npj Comput. Mater. **6,** 130 (2020).
9. R. S. Weis and T. K. Gaylord, Appl. Phys. A **37,** 191 (1985).
10. D. Janner, D. Tulli, M. Garcia-Granda, M. Belmonte, and V. Pruneri, Laser Photonics Rev. **3,** 301 (2009).
11. L. Chen, Q. Xu, M. G. Wood, and R. M. Reano, Optica **1,** 112 (2014).
12. M. He, M. Xu, Y. Ren, J. Jian, Z. Ruan, Y. Xu, S. Gao, S. Sun, X. Wen, L. Zhou, L. Liu, C. Guo, H. Chen, S. Yu, and X Cai, Nat. Photonics **13,** 359 (2019).
13. C. Xiong, W. H. P. Pernice, J. H. Ngai, J. W. Reiner, D. Kumah, F. J. Walker, C. H. Ahn, and H. X. Tang, Nano Lett. **14,** 1491 (2014).
14. S. Abel, T. Stöferle, C. Marchiori, C. Rossel, M. D. Rossell, R. Erni, D. Caimi, M. Sousa, A. Chelnokov, B. J. Offrein and J. Fompeyrine, Nat. Commun. **4,** 1671 (2013).
15. C. Dubourdieu, J. Bruley, T. M. Arruda, A. B. Posadas, J. Jordan-Sweet, M. M. Frank, E. Cartier, D. J. Frank, S. V. Kalinin, A. A. Demkov, and V. Narayanan, Nat. Nanotechnol. **8,** 748 (2013).
16. J. Nordlander, F. Eltes, M. Reynaud, J. Nürnberg, G. De Luca, D. Caimi, A. A. Demkov, S. Abel, M. Fiebig, J. Fompeyrine, and M. Trassin, Phys. Rev. Mater. **4,** 034406 (2020).
17. M. -H. M. Hsu, D. V. Thourhout, M. Pantouvaki, J. Meersschaut, T. Conard, O. Richard, H. Bender, P. Favia, M. Vila, R. Cid, J. Rubio-Zuazo, G. R. Castro, J. V. Campenhout, P. Absil, and C. Merckling, App. Phys. Express **10,** 065501 (2017).
18. W. Guo, A. B. Posadas, and A. A. Demkov, J. Vac. Sci. Technol. A **39,** 030804 (2021).
19. K. J. Kormondy, Y. Popoff, M. Sousa, F. Eltes, D. Caimi, M. D. Rossell, M. Fiebig, P. Hoffmann, C. Marchiori, M. Reinke, M. Trassin, A. A. Demkov, J. Fompeyrine, and S. Abel., Nanotechnology **28,** 075706 (2017).
20. A. A. Demkov and A. B. Posadas, MRS Bulletin (2022).
21. P. Castera, D. Tulli, A. M. Gutierrez, and P. Sanchis, Opt. Express **23,** 15332 (2015).
22. L. Cai, R. Kong, Y. Wang, and H. Hu, Opt. Express **23,** 29211 (2015).
23. W. Pompe, X. Gong, Z. Suo, and J. S. Speck, J. Appl. Phys. **74,** 6012 (1993).

24. J. S. Speck, and W. Pompe, J. Appl. Phys. **76,** 466 (1994).
25. R. A. McKee, F. J. Walker, and M. F. Chisholm, Phys. Rev. Lett. **81,** 3014 (1998).
26. F. Amy, A. S. Wan, A. Kahn, F. J. Walker, and R. A. McKee, J. Appl. Phys. **96,** 1635 (2004).
27. Y. Wei, X. Hu, Y. Liang, D. C. Jordan, B. Craigo, R. Droopad, Z. Yu, A. A. Demkov, J. L. Edwards Jr, and W. J. Ooms, J. Vac. Sci. Technol. B **20,** 1402 (2002).
28. K. D. Frederickson, H. Seo, and A. A. Demkov, J. Appl. Phys. **120,** 065301 (2016).
29. See Supplemental Material at [Insert URL here] for more theoretical considerations and supporting experimental details.
30. P. Zaumseil, J. Appl. Crystallogr. **48,** 528 (2015).
31. M. Reynaud, P. Y. Chen, W. Li, T. Paoletta, S. Kwon, D. H. Lee, I. Beskin, A. B. Posadas, M. J. Kim, C. M. Landis, K. Lai, J. G. Ekerdt., and A. A. Demkov, Phys. Rev. Mater. **5,** 035201 (2021).
32. Humboldt University – Structure Research and Electron Microscopy Group, "Useful plugins and scripts for Digital Micrograph." https://www.physik.hu-berlin.de/en. https://www.physics.hu-berlin.de/en/sem/software/software_frwrtools. (accessed November 22, 2021).
33. M. J. Hÿtch, J. -L. Putaux, and J. -M. Penisson, Nature **423,** 270 (2003).
34. V. Vaithyanathan, J. Lettieri, W. Tian, A. Sharan, A. Vasudevarao, Y. L. Li, A. Kochhar, H. Ma, J. Levy, P. Zschack, J. C. Woicik, L. Q. Chen, V. Gopalan, and D.G. Schlom, J. Appl. Phys. **100,** 024108 (2006).
35. J. A. Bland, Can. J. Phys. **37,** 417 (1959).
36. Y. Okada, and Y. Tokumaru, J. Appl. Phys. **56,** 314 (1984).
37. Y. L. Li, L. E. Cross, and L. Q. Chen, J. Appl. Phys. **98,** 064101 (2005).
38. Y. L. Li, and L.Q. Chen, Appl. Phys. Lett. **88,** 072905 (2006).
39. A. Y. Woldman, and C. M. Landis, Int. J. Solids Struct. **178-179,** 19 (2019).
40. A.Y. Woldman, PhD Thesis., University of Texas, Austin, 2017.
41. A. Yariv and P. Yeh, *Optical Waves in Crystals* (Wiley Interscience, New York, 1984), Chap. 7.
42. M. Zgonik, P. Bernasconi, M. Duelli, R. Schlesser, P. Günter, M. H. Garrett, D. Rytz, Y. Zhu, and X. Wu, Phys. Rev. B **50,** 5941 (1994).
43. S. Abel, D. Caimi, M. Sousa, T. Stöferle, C. Rossel, C. Marchiori, A. Chelnokov, and J. Fompeyrine, Proc. SPIE **8263,** 82630Y (2012).
44. S. H. Wemple, M. Didomenico Jr., and I. Camlibel, J. Phys. Chem. Solids **29,** 1797 (1968).
45. B. E. A. Saleh and M. C. Teich, *Fundamentals of Photonics* (John Wiley & Sons, 1991), Chap. 18.

Tables

Table I: Lattice constants from XRD peaks

Out-of-plane/In-plane	Peak	002/200 Region Lattice constant (Å)	004/400 Region Lattice constant (Å)
Out-of-plane	Strained c-axis	$4.049 \pm .002$	$4.048 \pm .002$
Out-of-plane	Relaxing c/a-axis	$4.024 \pm .001$	$4.024 \pm .001$
Out-of-plane	a-axis	$4.020 \pm .001$	$4.019 \pm .001$
In-plane	004	n/a	$4.014 \pm .007$
In-plane	400	n/a	$3.994 \pm .007$

Table II: Compared $V_\pi L$ values normalized by gap size

Work	Gap size (μm)	$V_\pi L / \text{gap size}$
This work	8	.19
Abel et al. [7]	4.75	.10
Xiong et al. [13]	2.8	.54

Figures

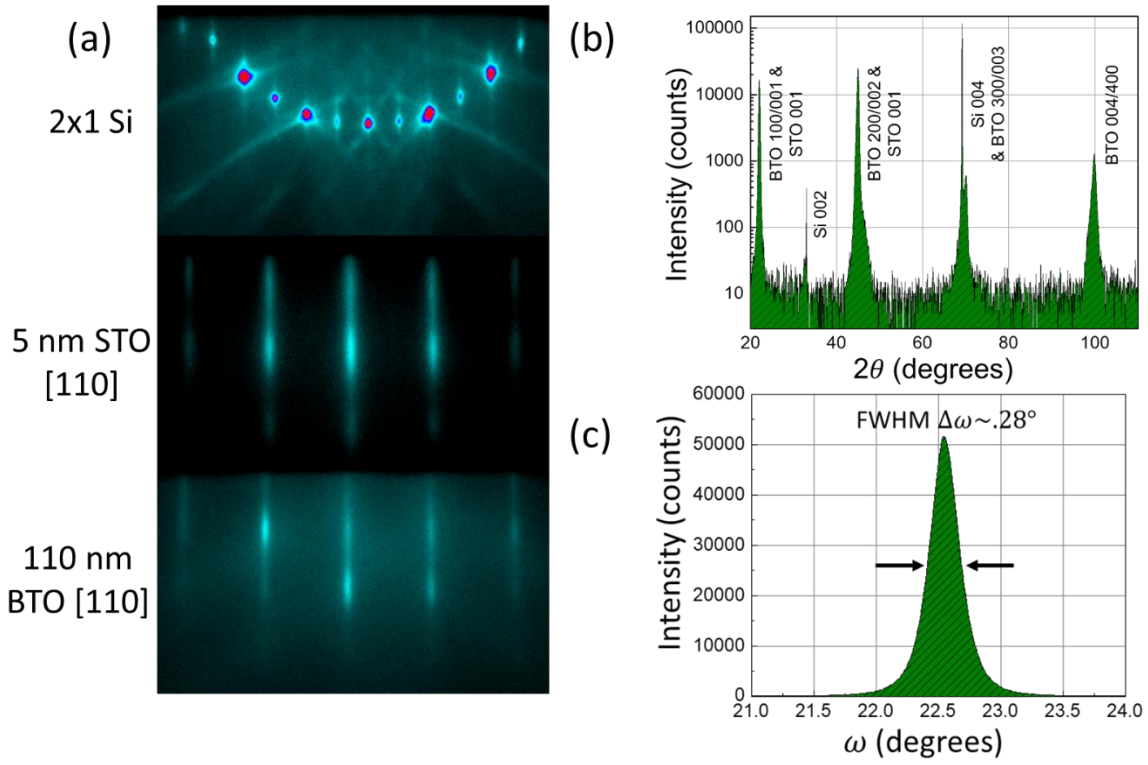

Figure 1: General characterization of BTO on STO-buffered Si. (a) RHEED of multiple stages of the growth of BTO, including the 2x1 reconstruction of the Si surface seen along the [110] direction along Si, and the [110] direction of both STO and BTO surfaces. (b) Out of plane XRD of the $BaTiO_3$ film, showing the film is in the expected phase. (c) Rocking curve of the BTO 002/200 peak.

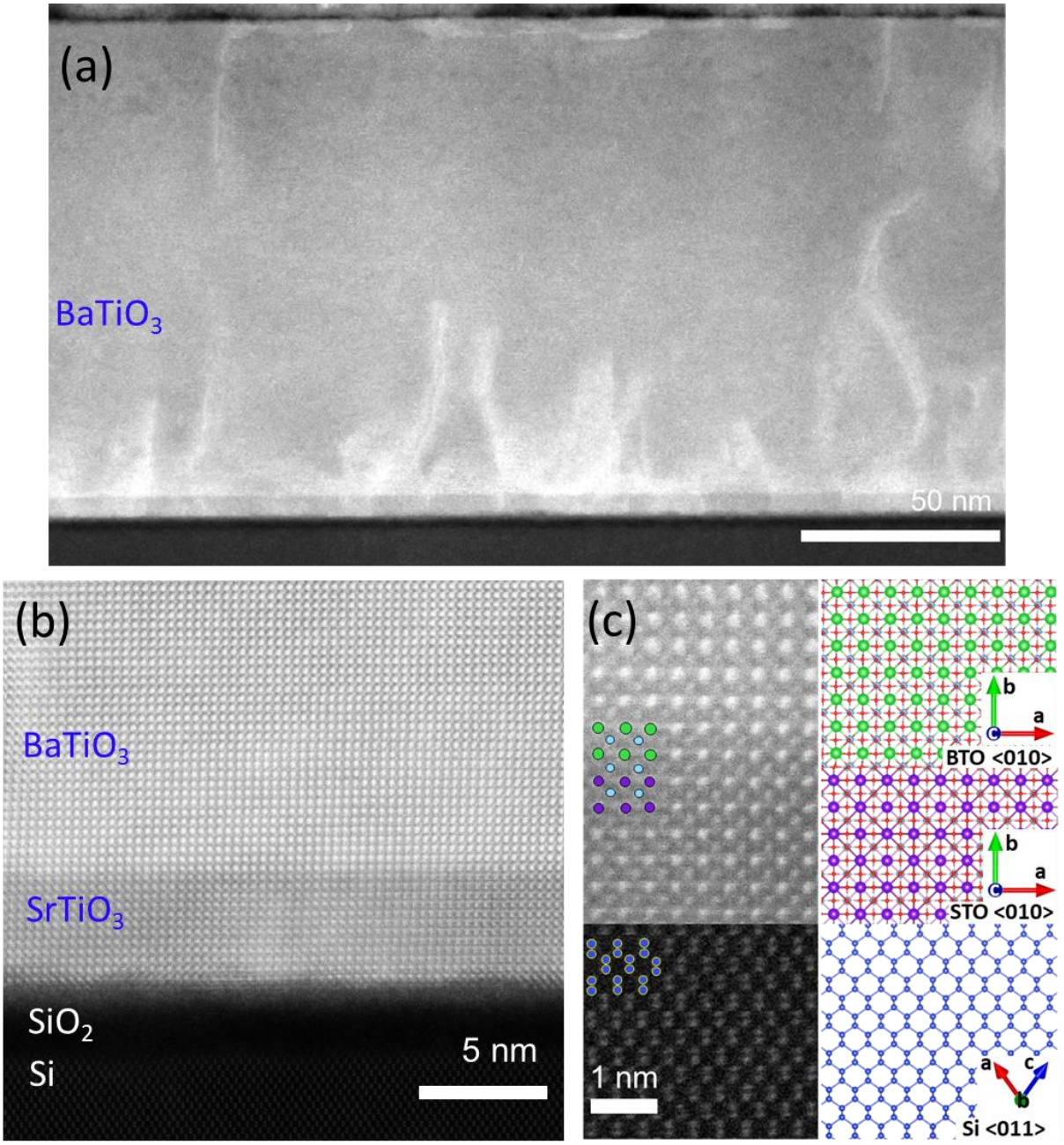

Figure 2: ADF-STEM imaging of thick BTO films. (a) Large scale image of BTO film showing no distinct grains and high epitaxy quality across the film. (b) Zoom in image showing the interfaces of the heterostructure. (c) Magnified zoom of interface region (excluding SiO_2) showing atomic scale epitaxy.

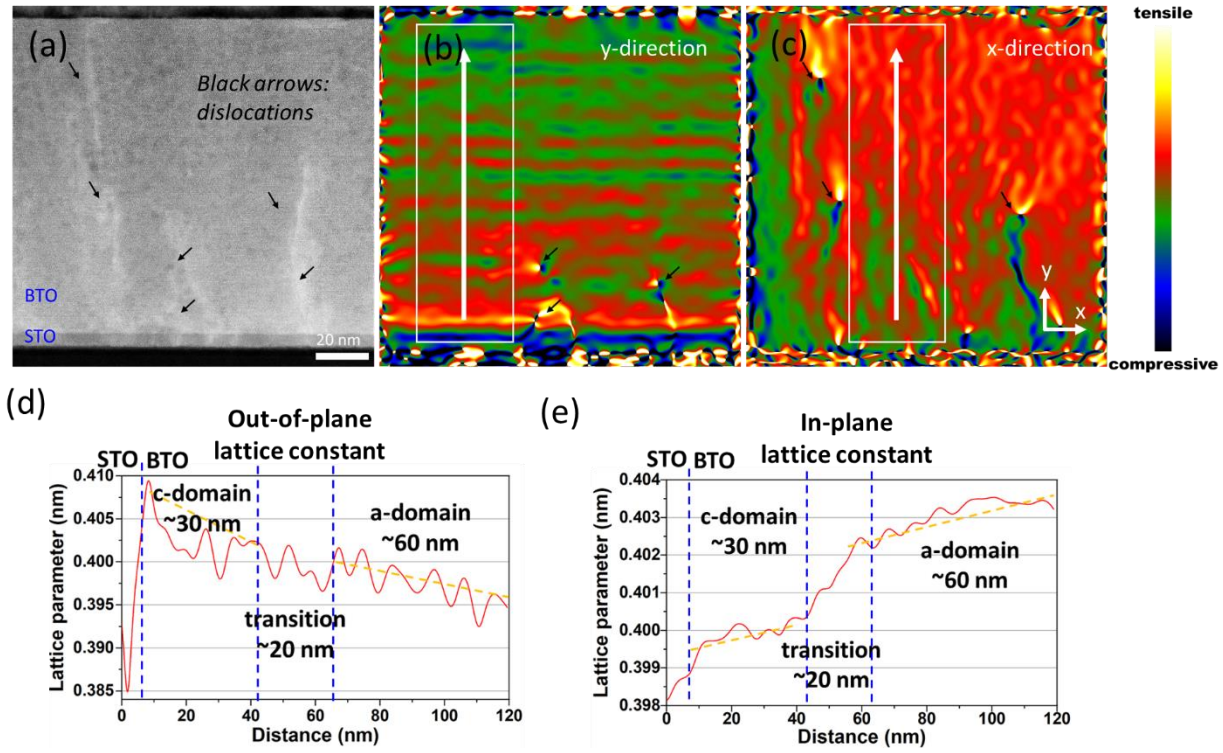

Figure 3: Geometric phase analysis of BTO film. (a) ADF-STEM image showing region where analysis is performed. (b-c) Strain profiles in the *x*- and *y*-direction, along with a box indicating the region where lattice constants are extracted. (d-e) Lattice constants in the out-of-plane direction (d) and in-plane direction (e).

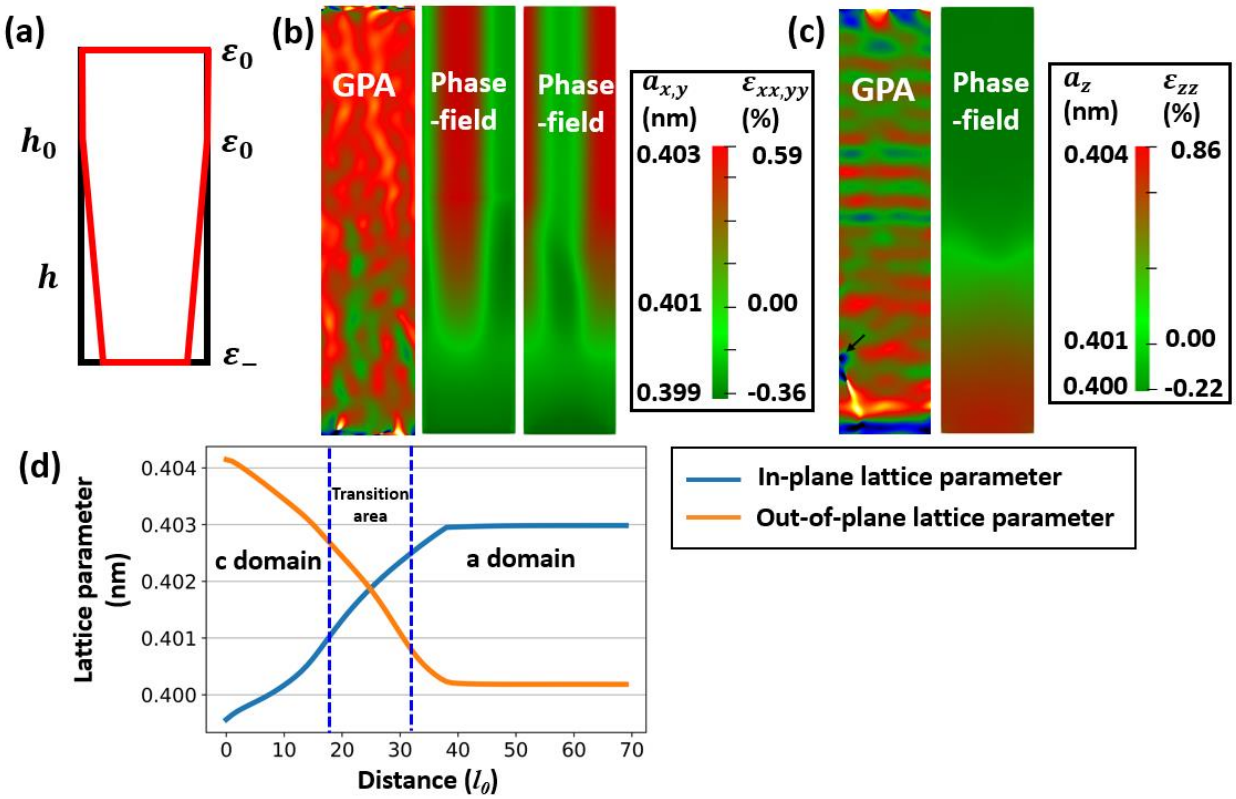

Figure 4: (a) Linear strain relaxation model. The black box represents an unstrained BTO film, while the red represents the strain profile of the BTO thin film. ε_0 is the strain in BTO near the surface and ε_- is the compressive strain near the BTO/STO interface. The simulation cell size is $(16 \times 16 \times 70)l_0$, where l_0 is the normalized unit length in our PFSs. h is the thickness of the entire cell, and h_0 is the thickness of compressively strained BTO. Additional details can be found in the Supplemental Material Note II [29]. (b)-(c) Crystallographic domain morphology, where the bottom is the BTO/STO interface and top is the BTO open surface. $a_{x,y}$ is the in-plane lattice constant (perpendicular to the growth direction z) and a_z the out-of-plane lattice constant (along the growth direction z). We also include the experimental strain profiles from Fig. 3 for a side-by-side comparison. (d) Plane averaged in-plane and out-of-plane lattice parameters along the z direction.

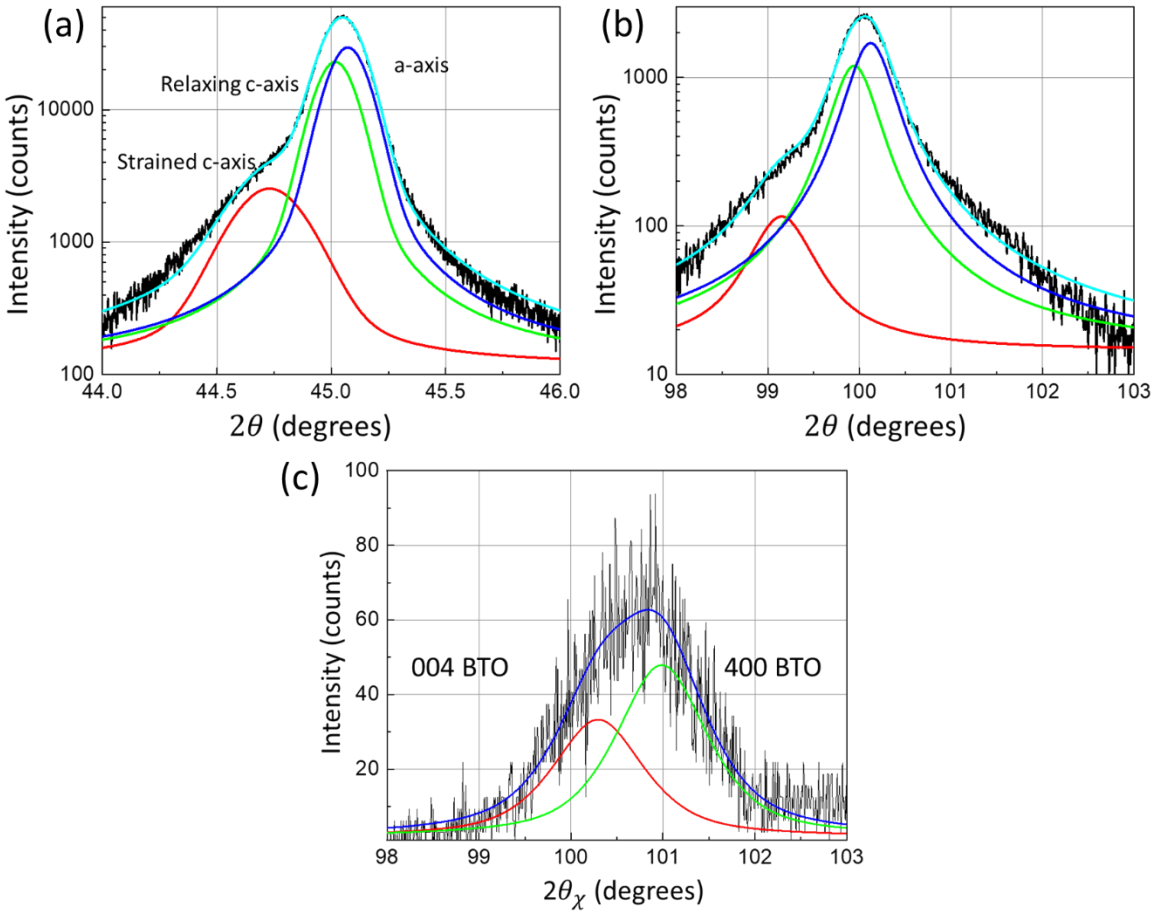

Figure 5: Fine scan out-of-plane and in-plane x-ray diffraction of BTO films. (a) Out-of-plane 002/200 region scan and (b) 004/400 region scan. (c) In-plane 004/400 region scan.

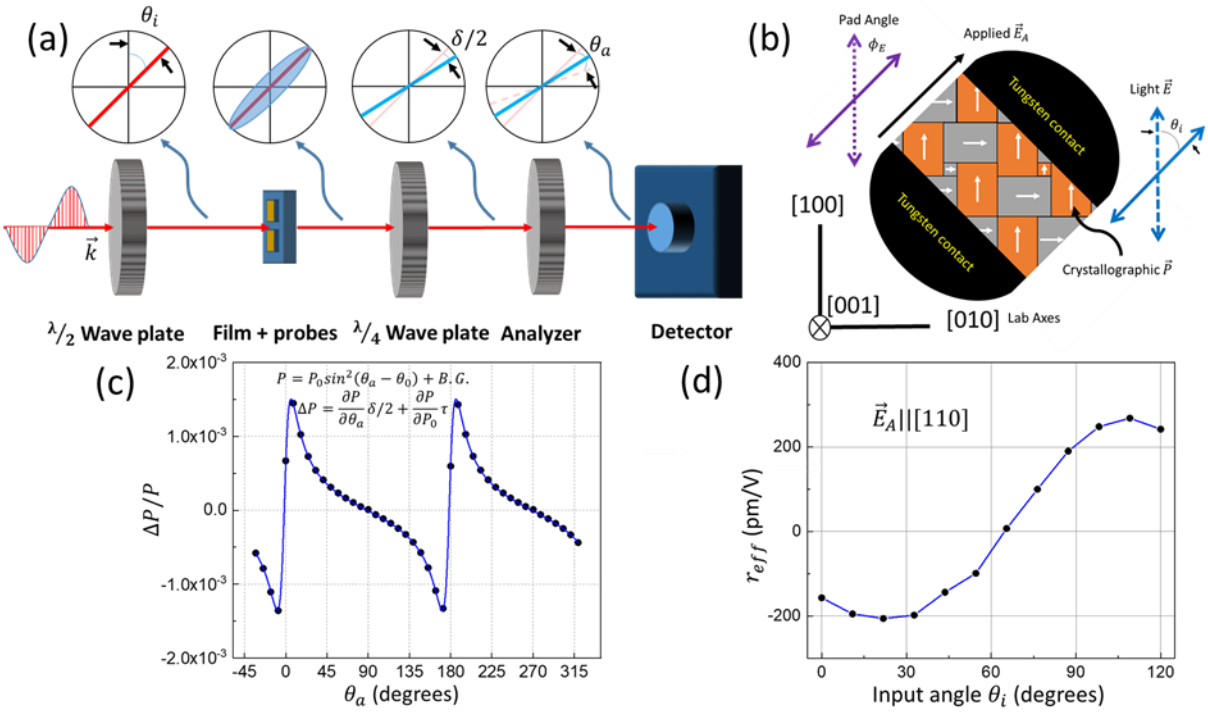

Figure 6: Pockels analysis of the film. (a) Schematic of setup. (b) Important quantities for measurement. (c) Example fit of Pockels data, showing the fit $\Delta P/P$ for a measurement, which can be used to extract $\delta/2$. (d) r_{eff} vs input angle for a 45° pad, showing clear input angle modulation on the Pockels coefficient.

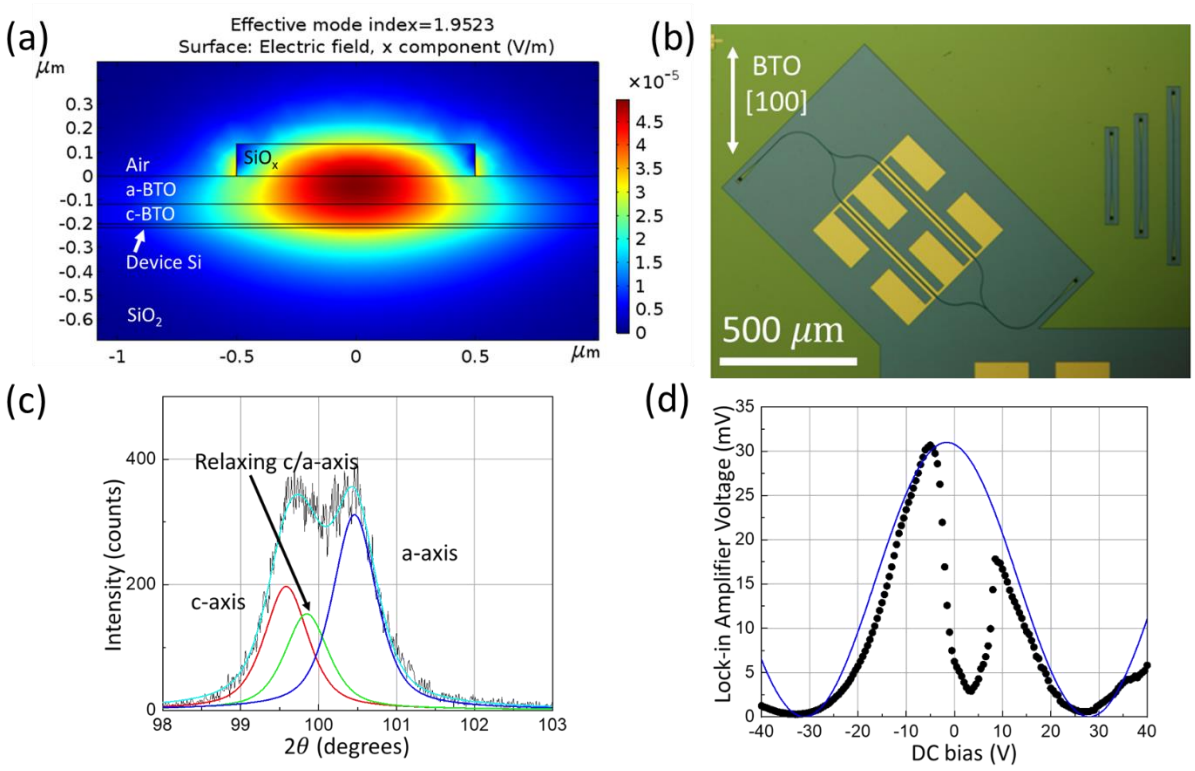

Figure 7: Waveguide measurements. (a) COMSOL simulation showing confinement of mode in the waveguide structure. (b) Image of the waveguide structures. (c) XRD fitting of 004/400 region for the 200 nm thick film. (d) Modulation of light through Mach-Zehnder interferometer compared with ideal behavior.